Practical joint domain localised adaptive processing in homogeneous and nonhomogeneous environments. Part 1: Homogeneous environments

R.S.Adve, T.B.Hale and M.C.Wicks

Abstract: This two-part paper presents a comprehensive approach to practical space–time adaptive processing (STAP) for airborne phased array applications. Part 1 reformulates the JDL algorithm to remove restrictions placed by the original development for ideal linear arrays of point sensors. In doing so the performance of the JDL algorithm is significantly improved in simulations and in measured data. The paper deals with STAP in homogeneous and non-homogeneous environments with Part 1 focusing on homogeneous environments and Part 2 dealing with STAP within range cells determined to be nonhomogeneous. Part 1 deals with applying the previously proposed joint domain localised (JDL) algorithm to practical phased arrays. Part 2 introduces a new STAP algorithm for application in nonhomogeneous interference scenarios. The algorithm is a hybrid of direct data domain and statistical adaptive processing.

1 Introduction

Airborne surveillance radar systems operate in a severe and dynamic interference environment. The interference may be deliberate (jamming) or clutter. The ability to detect weak targets, such as slow and small aircraft, requires the suppression of the interference in real time. Space–time adaptive processing (STAP) techniques promise to be the best means to suppress such interference.

Consider a phased array antenna with N spatial channels, possibly subarrays of a larger array, with M pulses per coherent processing interval (CPI). The most straightforward STAP algorithm uses all NM degrees of freedom (DOF). The algorithm estimates the NM dimensional covariance matrix of the interference to minimise the expected squared error with respect to the desired signal [1]. In practice, an accurate estimate requires about $2NM$ to $3NM$ independent, identically distributed (i.i.d.) secondary data samples [2]. Obtaining such a large number of i.i.d. samples is difficult, if not impossible. Furthermore, even if i.i.d. samples are available, the associated computation expense makes this fully adaptive algorithm impractical.

To overcome the drawbacks of the fully adaptive algorithm, researchers have limited the number of adaptive weights so as to reduce problems associated with sample support and computation expense. Wang and Cai [3] introduced the joint domain localised (JDL) algorithm, a post-Doppler, beamspace approach that adaptively processes the radar data after transformation to the angle–Doppler domain. Adaptive processing is restricted to a localised processing region (LPR) in the transform domain, significantly reducing the DOF while retaining maximal gain against thermal noise. The reduced DOF leads to corresponding reductions in required sample support and computation load.

In developing the JDL algorithm, the authors assume the receiving antenna to be an equi-spaced linear array of ideal, isotropic, point sensors. Based on this assumption, space–time data is transformed to the angle–Doppler domain using a two dimensional discrete Fourier transform (DFT). Under certain restrictions, this approach is valid because the spatial and temporal steering vectors form Fourier coefficients ([4], pp. 12–17). Due to the orthonormality of the DFT, the look space–time steering vector is localised to a single point in the angle–Doppler domain.

The use of a 2-D DFT restricts the spacing between angle/Doppler bins and the possible look directions/velocities. Without zero padding, the DFT can form only N orthogonal angle beams and M orthogonal Doppler beams. If the look direction matches one of these N angle beams and the look Doppler matches one of these M Doppler beams, the look steering vector is a column of the 2-D DFT matrix, which is orthogonal to the other columns of the matrix. The transformation therefore localises the look steering vector to a single bin in the angle–Doppler domain. To maintain the localisation of the target, the use of a window to suppress transform sidelobes is discouraged. For a small array, the beams are widely spaced in angle with correspondingly reduced correlation between beams. For a large array, the beams are spaced too close together with little information gained with each additional beam resulting in very high beam to beam correlation.

When applying the JDL algorithm to measured data, a crucial assumption in the development of [3] is invalid. The elements of a real array cannot be point sensors. Owing to their physical size, the elements of the array

IEE Proceedings online no. 20000035

DOI: 10.1049/ip-rsn:20000035

Paper first received 24th March and in revised form 25th October 1999

The authors are with the Air Force Research Laboratory, Sensors Directorate, Signal Processing Branch, 26 Electronic Parkway, Rome, NY 13441-4514, USA

are subject to mutual coupling. Furthermore, the assumption of a linear array is restrictive. A planar array allows for degrees of freedom in azimuth and elevation. Therefore the Fourier coefficients do not form the spatial steering vector and a DFT does not transform the spatial data to the angle domain. In this case, a DFT is mathematically feasible but has no physical meaning.

In a physical array, the spatial steering vectors must be measured or obtained using a numerical electromagnetic analysis. These steering vectors must be used to transform the space domain to the angle domain. This transformation is necessarily non-orthogonal with a corresponding spread of target information in the angle–Doppler domain. Earlier attempts to apply JDL to a real array ignored the non-orthogonal nature of the measured spatial transform [5].

This paper develops the JDL algorithm as applied to the case of an ideal array and serves to clarify the original development of the JDL algorithm as proposed by Wang and Cai [3], inorder to highlight the restrictions placed on the algorithm by the original formulation. The JDL algorithm is reformulated in terms of a transformation matrix which eliminates the restrictions on the JDL algorithm, and the DFT based formulation becomes a special, not necessarily optimal, case. Examples are presented illustrating the improvement in processing performance obtained by the new formulation, using simulated data for a linear array of isotropic sensors and measured data from the MCARM database [6].

Italicised letters denote scalars and integers, such as x and N, and lower case bold italic characters denote column vectors, e.g. $\boldsymbol{x}$. Upper case bold italic characters such as $\boldsymbol{R}$ denote matrices, while subscripts to bold characters represent the entries in the vector or matrix, such as $\boldsymbol{R}_{nm}$.

2 Joint domain localised processing

Consider an equispaced linear array of N isotropic, point sensors as shown in Fig. 1. Each channel receives M data samples corresponding to the M pulses in a CPI. Therefore, for each range bin the received data is a length MN vector $\boldsymbol{x}$ whose entries numbered mN to $[(m+1)N-1]$ correspond to the returns at the N elements from pulse number m, where $m=0, 1, \ldots, M-1$. The data vector is a sum of the contributions from the external interference sources, the thermal noise and possibly a target, i.e.

$$\boldsymbol{x} = \xi \boldsymbol{v}(\phi_t, f_t) + \boldsymbol{c} + \boldsymbol{n} \tag{1}$$

where $\boldsymbol{c}$ is the vector of interference sources, $\boldsymbol{n}$ is the thermal noise and ξ is the target amplitude, equal to zero in range cells without a target. The term $\boldsymbol{v}(\phi_t, f_t)$ is the space–time steering vector corresponding to a possible target at look angle ϕ_t and Doppler frequency f_t. Note that in STAP the steering vector sets the look direction where the target is assumed to be. In practice, there is some beam mismatch between the real target return and the steering vector. This

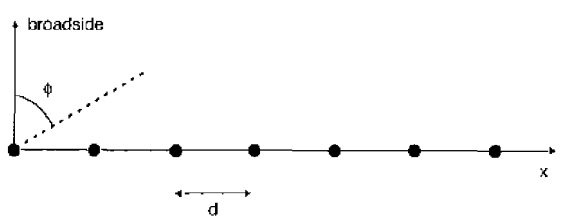

Fig. 1 *Linear array of point sensors*

steering vector can be written in terms of a spatial steering vector $\mathbf{a}(\phi_t)$ and a temporal steering vector $\mathbf{b}(f_t)$ [4],

$$\boldsymbol{v}(\phi_t, f_t) = \boldsymbol{b}(f_t) \otimes \boldsymbol{a}(\phi_t) \tag{2}$$

$$\boldsymbol{a}(\phi_t) = \left[1 \;\; e^{j2\pi f_s} \;\; e^{j(2)2\pi f_s} \;\; \ldots \;\; e^{j(N-1)2\pi f_s}\right]^T \tag{3}$$

$$\boldsymbol{b}(f_t) = \left[1 \;\; e^{j2\pi f_t/f_R} \;\; e^{j(2)2\pi f_t/f_R} \;\; \ldots \;\; e^{j(M-1)2\pi f_t/f_R}\right]^T \tag{4}$$

where $\otimes$ represents the Kronecker product of two vectors, f_s the normalised spatial frequency given by $(d/\lambda)\sin\phi_t$, λ the wavelength of operation and f_R the pulse repetition frequency (PRF).

The spatial steering vector $\boldsymbol{a}(\phi)$ is the magnitude and phase taper received at the N elements of the array due to a far field source at angle ϕ. Owing to electromagnetic reciprocity, to transmit in the direction ϕ the elements of the array must be excited with the conjugates of the steering vector, i.e. the conjugates of the steering vector maximize the response in the direction ϕ. Transformation of spatial data to the angle domain at angle ϕ therefore requires an inner product with the corresponding spatial steering vector. Similarly, the temporal steering vector $\boldsymbol{b}(f)$ corresponding to a Doppler frequency f is the magnitude and phase taper measured at an individual element for the M pulses in a CPI. An inner product with the corresponding temporal steering vector transforms time domain data to the Doppler domain. The angle–Doppler response of the data vector $\boldsymbol{x}$ at angle ϕ and Doppler f is therefore given by

$$\tilde{x}(\phi, f) = [\boldsymbol{b}(f) \otimes \boldsymbol{a}(\phi)]^H \boldsymbol{x} \tag{5}$$

where the tilde ($\sim$) above the scalar x signifies the transform domain. Choosing a set of spatial and temporal steering vectors generates a corresponding vector of angle–Doppler domain data.

Eqns. 2–4 show that for an ideal array the spatial and temporal steering vectors are identical to the Fourier coefficients. Based on this observation, the transformation to the angle–Doppler domain can be simplified under two conditions.

(i) If a set of angles are chosen such that $(d/(\lambda \sin\phi))$ is spaced by $1/N$ and a set of Doppler frequencies are chosen such that (f/f_R) is spaced by $1/M$, the transformation to the angle-Doppler domain is equivalent to the 2-D DFT.
(ii) If the look angle ϕ_t corresponds to one these angles and the look Doppler f_t corresponds to one of these Dopplers, the steering vector is a column of the 2-D DFT matrix and the angle–Doppler steering vector is localised to a single angle–Doppler bin.

The JDL algorithm as originally developed in [3] assumes both these conditions are met. This simplification is possible only in the case of the ideal, equispaced, linear array of Fig. 1. Owing to beam mismatch, the localisation to a single point in angle–Doppler space is only exact for the look steering vector.

As shown in Fig. 2, a LPR centred about the look angle–Doppler point is formed and interference is suppressed in this angle–Doppler region only. The LPR covers η_a angle bins and η_d Doppler bins. The choice of η_a and η_d is independent of N and M, i.e. the localisation of the target to a single angle–Doppler bin decouples the number of adaptive degrees of freedom from the size of the data cube, while retaining maximal gain against thermal noise. The covariance matrix corresponding to this LPR is estimated using secondary data from neighbouring range cells. The adaptive weights are then calculated by

$$\tilde{\boldsymbol{w}} = \tilde{\boldsymbol{R}}^{-1}\tilde{\boldsymbol{v}} \tag{6}$$

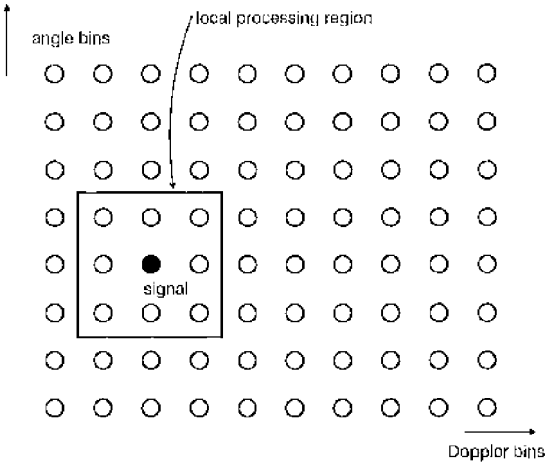

Fig. 2 *Localised processing regions in joint domain localised processing for* $\eta_a = \eta_d = 3$

where $\tilde{\boldsymbol{R}}$ is the estimated angle–Doppler covariance matrix corresponding to the LPR of interest. The number of adaptive unknowns is equal to $\eta_a \eta_d$. The steering vector for the adaptive process is represented by $\tilde{\boldsymbol{v}}$ and is the space–time steering vector $\boldsymbol{v}$ of eqn. 2 transformed to the angle–Doppler domain. Under the two conditions listed above, $\tilde{\boldsymbol{v}}$ is given by the length $\eta_a \eta_d$ vector

$$\tilde{\boldsymbol{v}} = [0, 0, \ldots, 0, 1, 0, \ldots, 0, 0]^T \tag{7}$$

It must be emphasised that this simple form of the steering vector is valid only because the DFT is an orthogonal transformation and the space–time steering vector is transformed to the angle–Doppler domain using the same transformation as used for the data.

The adaptive weights of eqn. 6 are used to find a statistic for detection by hypothesis testing. This paper uses the modified sample matrix inversion (MSMI) statistic [7]

$$\rho_{\mathrm{MSMI}} = \frac{|\tilde{\boldsymbol{w}}^H \tilde{\boldsymbol{x}}_{\mathrm{LPR}}|^2}{\tilde{\boldsymbol{w}}^H \tilde{\boldsymbol{R}} \tilde{\boldsymbol{w}}} \tag{8}$$

where $\tilde{\boldsymbol{x}}_{\mathrm{LPR}}$ is the length $\eta_a \eta_d$ angle–Doppler data vector from the LPR and range cell of interest.

3 JDL processing based on a transformation matrix

As developed by Wang and Cai [3], the JDL algorithm assumes a linear array of point sensors and the two conditions listed in Section 2. These conditions, though not explicitly stated in [3], restrict the choice of spacing between angle–Doppler bins in the transform domain and also the allowed look directions.

The most significant problem with the JDL algorithm described in Section 2 is that the assumption of an array of point sensors cannot be satisfied in practice. Each array element must have a non-zero physical size leading to mutual coupling between the elements. Furthermore, the assumption of a linear array is overly restrictive. Real arrays may be planar to allow for degrees of freedom in azimuth and elevation. In practice, the spatial steering vectors are not the Fourier coefficients given by eqn. 3 and must be measured or obtained using a numerical electromagnetic analysis. The steering vectors so obtained can be used to transform the space domain to the angle domain. The continued use of a DFT is mathematically feasible, but the transform domain would not be the angle domain and would have no physical meaning.

This paper replaces the DFT-based transformation described in Section 2 with a general transformation matrix. The key contribution of this new approach is the elimination of the two stipulations on the original JDL algorithm of [3]. This formulation can be directly applied to both linear arrays of isotropic point sensors and physical arrays of arbitrary configuration. In both cases, the modifications can result in significantly improved detection performance.

In the JDL algorithm, only data from within the LPR is used for the adaptation process. Eqn. 5 indicates that the transformation from the space–time domain to the angle–Doppler domain is, in effect, an inner product with a space–time steering vector. This argument holds true for ideal linear arrays and physical arrays. Mathematically therefore, the relevant transformation to within the LPR is a pre-multiplication with a $(NM \times \eta_a \eta_d)$ transformation matrix. The transformation process is

$$\tilde{\boldsymbol{x}}_{\mathrm{LPR}} = \boldsymbol{T}^H \boldsymbol{x} \tag{9}$$

For example, based on eqn. 5, if the LPR covers 3 angle bins (ϕ_{-1}, ϕ_0, ϕ_1; $\eta_a = 3$) and 3 Doppler bins (f_{-1}, f_0, f_1; $\eta_d = 3$)

$$\begin{aligned}\boldsymbol{T} = [&\boldsymbol{b}(f_{-1}) \otimes \boldsymbol{a}(\phi_{-1}) \;\; \boldsymbol{b}(f_{-1}) \otimes \boldsymbol{a}(\phi_0) \;\; \boldsymbol{b}(f_{-1}) \otimes \boldsymbol{a}(\phi_1) \\ &\boldsymbol{b}(f_0) \otimes \boldsymbol{a}(\phi_{-1}) \;\; \boldsymbol{b}(f_0) \otimes \boldsymbol{a}(\phi_0) \;\; \boldsymbol{b}(f_0) \otimes \boldsymbol{a}(\phi_1) \\ &\boldsymbol{b}(f_1) \otimes \boldsymbol{a}(\phi_{-1}) \;\; \boldsymbol{b}(f_1) \otimes \boldsymbol{a}(\phi_0) \;\; \boldsymbol{b}(f_1) \otimes \boldsymbol{a}(\phi_1)] \end{aligned} \tag{10}$$

$$= [\boldsymbol{b}(f_{-1}) \;\; \boldsymbol{b}(f_0) \;\; \boldsymbol{b}(f_1)] \otimes [\boldsymbol{a}(\phi_{-1}) \;\; \boldsymbol{a}(\phi_0) \;\; \boldsymbol{a}(\phi_1)] \tag{11}$$

In [3], to achieve the simple form of the angle–Doppler steering vector given by eqn. 7, the use of a low sidelobe window to lower the transform sidelobes is discouraged. However, the use of a low sidelobe window may be incorporated by modifying the transformation matrix of eqn. 11. If a length N taper $\boldsymbol{t}_s$ is to be used in the spatial domain and a length M taper $\boldsymbol{t}_t$ in the temporal domain, the transformation matrix is given by

$$\begin{aligned}\boldsymbol{T} = &[\boldsymbol{t}_t \odot \boldsymbol{b}(f_{-1}); \;\; \boldsymbol{t}_t \odot \boldsymbol{b}(f_0); \;\; \boldsymbol{t}_t \odot \boldsymbol{b}(f_1)] \\ &\otimes [\boldsymbol{t}_s \odot \boldsymbol{a}(\phi_{-1}); \boldsymbol{t}_s \odot \boldsymbol{a}(\phi_0); \;\; \boldsymbol{t}_s \odot \boldsymbol{a}(\phi_1)] \end{aligned} \tag{12}$$

where $\odot$ represents the Hadamard product, a point-by-point multiplication of two vectors.

The angle–Doppler steering vector used to solve for the adaptive weights in eqn. 6 is the space–time steering vector $\boldsymbol{v}$ transformed to the angle–Doppler domain via the same transformation matrix $\boldsymbol{T}$, i.e.

$$\tilde{\boldsymbol{v}} = \boldsymbol{T}^H \boldsymbol{v} \tag{13}$$

Note the transformation matrix defined in eqn. 11 is defined for the chosen frequencies and angles without any restrictions on their values. Further, no assumption is made about the form of the spatial or temporal steering vectors, i.e. the use of a transformation matrix eliminates the two restrictions placed on the original JDL formulation.

In the case of a linear array of isotropic point sensors, the steering vectors are obtained from eqns. 3 and 4. If the angles and Doppler frequencies satisfy the conditions listed in Section 2, the transformation matrix $\boldsymbol{T}$ reduces to the relevant rows of the 2-D DFT matrix. The DFT-based formulation is equivalent to choosing a spacing in the angle domain such that $(d/\lambda)\Delta \sin\phi = 1/N$ and in the Doppler domain of $\Delta f = 1/M$. Furthermore, if both the look angle and Doppler correspond to one of these

angles and Dopplers, the transformed steering vector of eqn. 13 is equivalent to the steering vector of eqn. 7. The formulation of [3] is a special, not necessarily optimal, case of the more general formulation presented in this Section.

The steering vector associated with a given angle is the measured magnitude and phase taper due to a calibrated far-field source. If measurements are not available, the steering vectors can be obtained from a numerical electromagnetic analysis of the receiving antenna. Usually, even in the case of a real array, the pulses are equally spaced in time and hence the temporal steering vector is unchanged. In the case of a real array, the spatial component in eqn. 2 must be replaced with a measured steering vector, i.e.

$$v(\phi_t, f_t) = \boldsymbol{b}(f_t) \otimes \boldsymbol{a}_{\mathrm{m}}(\phi_t) \tag{14}$$

Similarly, the spatial steering vectors in the transformation matrix of eqns. 11 and 12 must be replaced with the corresponding measured steering vectors.

In Section 2, assuming both listed conditions are met and based on the orthogonality of the DFT, the target is localised to a single point in the angle–Doppler domain and the angle–Doppler steering vector reduces to the simple form in eqn. 7. This simplification is invalid once the two restrictions are relaxed and the target information is spread in the angle–Doppler domain. The use of eqn. 13 accounts for the resulting spread in target information.

Melvin and Himed [5] applied the JDL algorithm to measured data and used the measured steering vectors to transform the space domain to the angle domain. In effect, without explicitly stating so, they use a transformation matrix in the spatial domain and a DFT in the temporal domain. The spacing between the angles chosen for the LPR is determined by the available measured steering vectors. The spacing between the Doppler frequencies is fixed by the DFT. Crucially, the resulting change on the angle–Doppler steering vector ($\tilde{\boldsymbol{v}}$) is ignored and they assume the simplified form of the steering vector in eqn. 7 is valid. However, this is untrue since the use of a different transform from the spatial domain to the angle domain violates the assumptions on which eqn. 7 is based. Furthermore, the authors of [5] explicitly discourage the use of windows in the transformation.

4 Numerical examples

In this Section, four examples illustrate the improvement in adaptive performance gained by taking the non-orthogonal nature of the spatial steering vectors into account. The examples also illustrate the use of a windowed transformation from the space–time domain to the angle–Doppler domain. Two of the examples presented use simulated data based on an ideal linear array of point sensors. The other two examples use measured data from the multi-channel airborne radar measurements (MCARM) [6] database.

4.1 Simulated data

The formulation presented in Section 3 removed the restrictions placed by the original development of the JDL algorithm in [3]. This Section presents two examples to illustrate the improvements in detection performance.

The examples use simulated data based on an ideal linear array of isotropic point sensors. The models used to generate the data are briefly explained below in Section 4.1.1. The detection performance is illustrated by plotting the probability of detection (P_d), obtained using a Monte Carlo simulation, as a function of the target signal-to-noise ratio for a chosen probability of false alarm (P_{fa}). The MSMI statistic of eqn. 8 is used. This statistic has a constant false alarm rate (CFAR) in that, given Gaussian interference, P_{fa} is only dependent on the chosen threshold.

In each of the examples presented, the P_d is evaluated for two cases: the DFT based JDL algorithm of [3] and the formulation presented in this paper. The second case shows that the spacing between angle and Doppler bins in the transform domain may be chosen independently of the number of elements and pulses. In this paper the spacing in the angle is chosen to be a fraction of the spacing dictated by the DFT-based formulation.

4.1.1. Data models: These examples use a data cube containing the simulated returns of clutter and target information by an airborne linear array of isotropic point sensors. The data generation scheme uses the physical model presented by Jaffer *et. al.* [8] and Ward [4].

The clutter is modelled as a sum of the contributions of many discrete far-field sources. In this paper, 181 discrete sources are used, spaced 1° apart. The amplitude of each source is a complex Gaussian random variable whose average power is set by a chosen clutter-to-noise ratio (CNR) and also weighted by the transmit beam pattern of the array. The normalised Doppler shift associated with each clutter source is set by the velocity of the array platform v_p and is given by ([4], p. 25)

$$f_c = \beta \cos \phi_c \tag{15}$$

$$\beta = \frac{2 v_p}{d f_R} \tag{16}$$

The parameter β is the number of half element spacings the platform traverses in one pulse interval. The contribution of a clutter patch at angle ϕ_c is therefore

$$c(\phi_c) = \alpha[\boldsymbol{b}(f_c) \otimes \boldsymbol{a}(\phi_c)] \tag{17}$$

where α is a weighted complex Gaussian random variable as described above. The sum of clutter contributions from all 181 angles forms the received clutter vector.

The thermal noise is modelled as a Gaussian white noise process. The average power is set to unity allowing for the clutter and target powers to be referenced to the white-noise power. These simulations do not include the effects of other interference sources such as jammers. As given in eqn. 1, in those range cells with a target the contribution of the target is given by $\xi v(\phi_t, f_t)$.

The examples using simulated data ignore other factors that affect STAP performance such as crab angle, mutual coupling and beam mismatch between target and steering vector. Table 1 lists the details of the array and interference scenario. The Table also lists the parameters used in the implementation of the JDL algorithm and the spacing between angle and Doppler bins in the formulation of the modified JDL algorithm developed in this paper.

4.1.2. Example 1. Half-wavelength spacing: This example uses data received by an 8-element array with 8 pulses per CPI. The spacing between array elements is $\lambda/2$. In the case of the DFT, the spacing between angle bins is set at $\Delta(\sin\phi) = 1/(0.5N) = 0.25$, i.e. the angle bins are spaced $\Delta\phi = 14.47°$ apart. This large spacing leads to uncorrelated beams. The new formulation uses a spacing of 7.24°, half that of the DFT case.

In this example 36 secondary data vectors are used to estimate the 9×9 angle–Doppler covariance matrix. For the MSMI CFAR statistic, the threshold for a false-alarm rate of 0.01 ($P_{fa} = 0.01$) is 8.35. This high false-alarm rate

Table 1: Parameters for examples 1 and 2

Parameter	Example 1	Example 2
Elements N	8	8
Pulses M	8	8
Element spacing	0.5λ	10λ
Pulse repetition frequency	1024 Hz	1024 Hz
Mainbeam transmit azimuth	0 deg	0 deg
Transmit array pattern	uniform	uniform
β	5.0	2.5
Number of clutter patches	181	181
Target normalised Doppler, f_t	1/3	1/3
Target azimuth, ϕ_t	0	deg
Thermal noise power	unity	unity
Clutter-to-noise ratio	50 dB	50 dB
Number of Doppler bins in LPR	3	3
Number of angle bins in LPR	3	3
Angle bin spacing-modified JDL	$1/2N$	$1/N\sqrt{2}$
Doppler bin spacing	$1/2M$	$1/M$

is chosen to reduce the number of trials required to obtain a reliable estimate of the probability of detection. The number of trials is chosen to be 9964.

Fig. 3 plots the probability of detection versus the signal-to-noise ratio for the above threshold. The solid curve is the P_d using the optimal weights obtained using the known space time covariance matrix. The other two curves compare the P_d using the formulation developed in this paper, with the P_d using the DFT-based JDL algorithm. As is seen, the probability of detection is significantly higher for the new formulation for the same signal-to-noise ratio and the same P_{fa}. The new formulation shifts the P_d curve to the left by approximately 4 dB, a significant improvement in detection performance.

4.1.3. Example 2. Large interelement spacing: The second example illustrates the working of the new formulation, using an array with a large interelement spacing of 10λ. The details of the array, the scenario and the parameters used in the implementation of the JDL algorithm

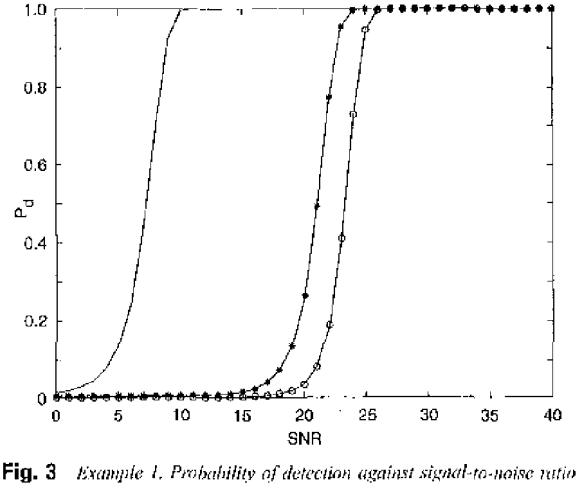

Fig. 3 *Example 1. Probability of detection against signal-to-noise ratio*
— — optimal
--*-- JDL-new
--○-- JDL-DFT

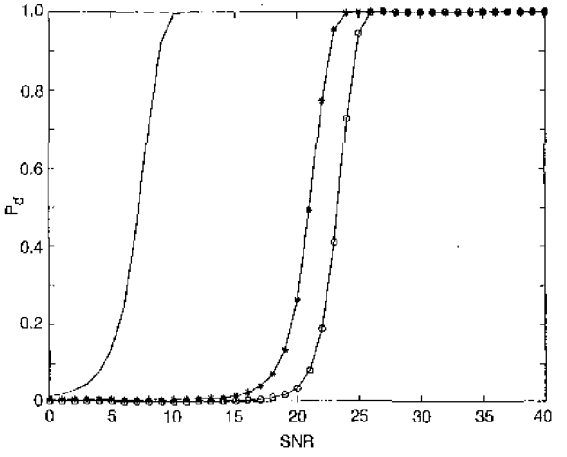

Fig. 4 *Example 2. Probability of detection against signal-to-noise ratio*
— — optimal
--*-- JDL-new
--○-- JDL-DFT

are listed in Table 1. Here the Doppler spacing chosen for the modified JDL algorithm is the same as in the case of using a DFT. As in Section 4.1.2, 9964 independent realisations are used to estimate the probability of detection.

Fig. 4 plots the probability of detection versus the signal-to-noise ratio for the same threshold as in Example 1. The solid curve is the P_d, using the optimal weights obtained by using the known covariance matrix. The other two curves compare the P_d, using the formulation developed in this paper with the P_d using the DFT-based JDL algorithm. For the same P_{fa}, the new formulation shifts the P_d curve to the left by approximately 2.5 dB.

It must be emphasised that this paper does not investigate the optimal spacing between angle and Doppler bins to maximise the performance of the JDL algorithm. The spacings used here represent just one possible choice. The choice of the optimal spacing between angles and Doppler bins in the transform domain is an open research problem.

4.2 Measured data from the MCARM database

This Section presents examples of the performance improvement gained using the formulation presented in this paper, as applied to measured data. The examples use data from the multi-channel airborne radar measurements (MCARM) [6] database, a vast collection of clutter and signal measurements collected by an airborne radar over multiple flights with multiple acquisitions on each flight. The acquisitions used in these examples use a 22-element rectangular array arranged in a 2×11 grid. Each CPI comprises 128 pulses ($M = 128$).

The database includes clutter measurements over different terrain and the returns from a target aircraft flying approximately parallel to the radar platform. Some acquisitions include the signals (tones) from a moving target simulator (MTS) of known Doppler shift and power. Also provided with the data is a set of measured spatial steering vectors for some specified azimuth and elevation angles. As explained in Section 3, these steering vectors are used in [5] and here for spatial processing of the data.

The two examples presented here illustrate the improvement in detection performance by accounting for the non-orthogonal nature of the steering vectors. For each example, three scenarios are compared. In the first two

scenarios, the space–time data is transformed using a DFT in time and the measured steering vectors in space. The first scenario ignores the target spreading due to the non-orthogonal nature of the spatial steering vectors. This is equivalent to using eqn. 11 to transform the space–time data to the angle–Doppler domain, but using eqn. 7 as the angle–Doppler steering vector. This approach has been used by [5].

The second scenario accounts for the non-orthogonality and so uses eqn. 13 to evaluate the angle–Doppler steering vector. The final scenario uses a window before transforming the time domain to the Doppler domain. This scenario uses eqn. 12 to evaluate the transformation matrix and eqn. 13 to evaluate the adaptive steering vector for JDL. This paper introduces for the first time the use of a window in the transformation. In all examples, 3 angle bins and 3 Doppler bins form the LPR and 36 secondary data vectors are used to estimate the angle–Doppler covariance matrix. The spatial steering vectors are measured at approximately 1° spacings. The covariance matrix of the interference is estimated using 18 secondary data cells on either side of the range bin of interest, neglecting the first range cell on each side as a guard cell. The MSMI statistic of eqn. 8 is used for detection.

In a radar system, a beam is transmitted in a particular direction and the returns are processed for targets in that direction only. Hence, while all Doppler frequencies of interest are examined, the angle bin of interest remains constant over the entire CPI. Therefore the adaptive steering vector of eqn. 13 can be calculated *a priori* for each CPI.

The performance of windowed JDL is sensitive to the choice of window. In [9], Harris compares the properties of many different possible windows. His figure of merit is the difference between the equivalent noise bandwidth and the normalised 3-dB bandwidth of the window. Using this criterion, he concludes that for fixed point arithmetic, the Kaiser–Bessel window is the top performer. The sidelobes of the Kaiser–Bessel window can be controlled by a parameter κ which is half the time-bandwidth product of the window. In this work, we use a 128-point Kaiser–Bessel window with $\kappa = \log(128)$ in the time domain. In the space domain, due to the limited number of elements available, the reduction in the mainbeam gain is significant even for shallow windows. Hence, a window is not used in the space domain.

4.2.1. Example 1. Injected target: In the first example, a fictitious target of chosen amplitude, direction and Doppler is added to the MCARM data at a particular range bin. The amplitude and phase taper of the injected target at each of the 22 channels is obtained from the measured steering vectors. The amplitude of the injected target is chosen such that it is too weak to be observed by non-adaptive digital beamforming. The JDL algorithm is used to detect the injected target by suppressing the clutter.

The JDL processing is performed at the target angle bin, for a few range bins surrounding the injected target, and for all Doppler bins. Since this example uses measured data, the figure of merit used to compare the three scenarios is the separation between the MSMI statistic at the target range/Doppler bin and the highest statistic at other range or Doppler bins. A large separation implies a large difference between target and residual interference, improving the ability to detect the target.

This example uses data from acquisition 575 on flight 5. The target parameters are

- amplitude (ξ) = 0.00003 ∠0
- angle bin = 0° ≡ broadside
- Doppler bin = −9
- range bin = 290

Unfortunately, the MCARM database does not clearly define the noise level of the antenna. Different approaches to evaluating the noise level have yielded significantly varying results. For the acquisition at hand, the noise floor has been estimated between −81 and −95 dB. Therefore the signal-to-noise ratio of the injected target before and after processing is not available.

Fig. 5. plots the MSMI statistic, at the broadside and target range bin, as a function of Doppler for the first scenario where non-orthogonality is ignored. The statistic at the target location is clearly visible over the surrounding clutter. However, the target is found at Doppler bin −8, not the expected −9. The separation between the statistic at bin −8 and the highest clutter statistic at bin −24 is 3.13 dB. The statistic at Doppler bin −9 is actually lower than the surrounding clutter. Fig. 6 plots the MSMI statistic as a function of range for Doppler bin −9. The target at range bin 290 is overwhelmed by the clutter at range bin 266 and the target is 8.73 dB below the clutter.

Fig. 7 shows the same plot when the non-orthogonal nature of the spatial steering is accounted for. The

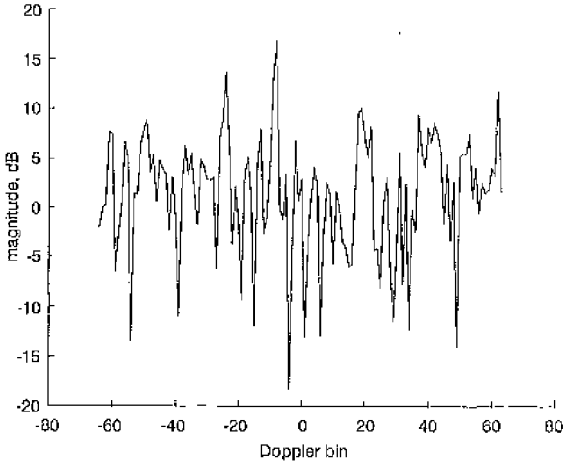

Fig. 5 *MSMI statistic against Doppler ignoring the non-orthogonality of the steering vectors*

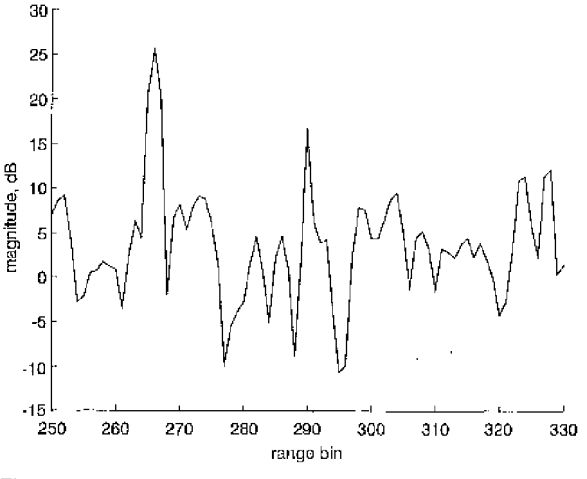

Fig. 6 *MSMI statistic against range ignoring the non-orthogonality*

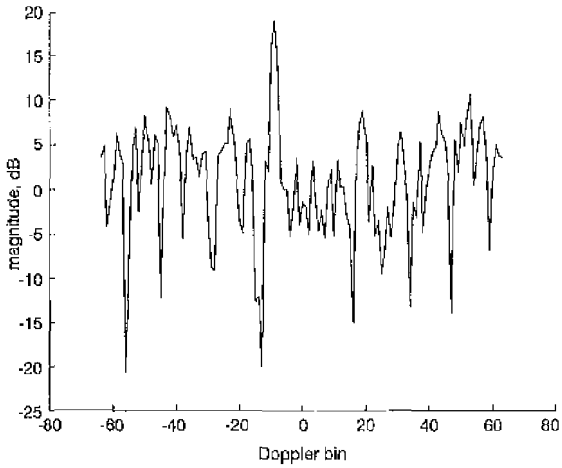

Fig. 7 *MSMI statistic against Doppler accounting for the non-orthogonality*

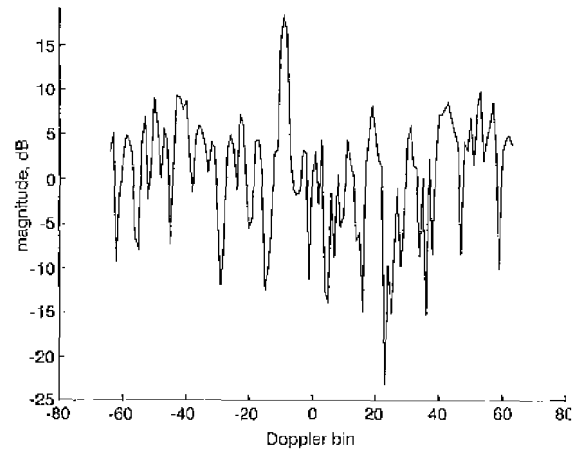

Fig. 9 *MSMI statistic against Doppler using a Kaiser–Bessel window*

improved detection performance is clearly visible with the peak in the correct Doppler bin of −9. The highest statistic at Doppler bin 53 is 8.39 dB below the statistic at the target. This is an improvement of 5.26 dB over the first scenario. Fig. 8 plots the MSMI statistic as a function of range at the target Doppler for the second case. Note that accounting for the non-orthogonality of the steering vectors makes the target stand out over the surrounding clutter. The statistic at the target range 290 is 2.49 dB over the highest clutter statistic at range bin 266. This is an improvement of 11.22 dB over the first case.

Fig. 9 plots the results when the Kaiser–Bessel window is used. The statistic is maximum at Doppler bin −9, showing a separation of 8.80 dB, and improvement of 5.67 dB over the first scenario and 0.41 dB over the second scenario. Fig. 10 plots the results versus range. Again, the target at range bin 290 stands out over the surrounding clutter. The separation over the highest clutter statistic is 3.13 dB, an improvement of 11.86 dB over the first scenario and 0.64 dB over the second scenario.

A summary of the results in Figs. 5–10 is presented in Table 2. The improvement listed is over the traditional JDL case.

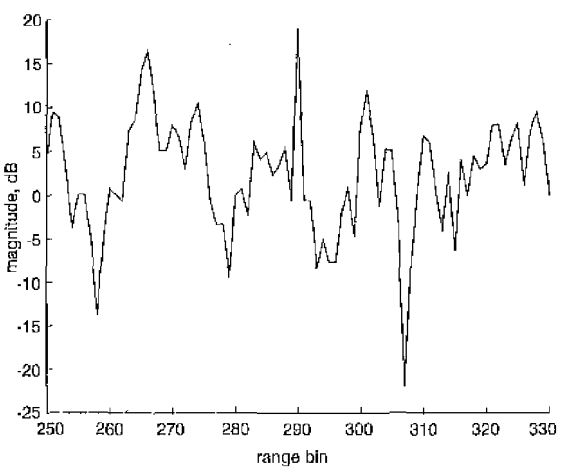

Fig. 8 *MSMI statistic against range accounting for the non-orthogonality*

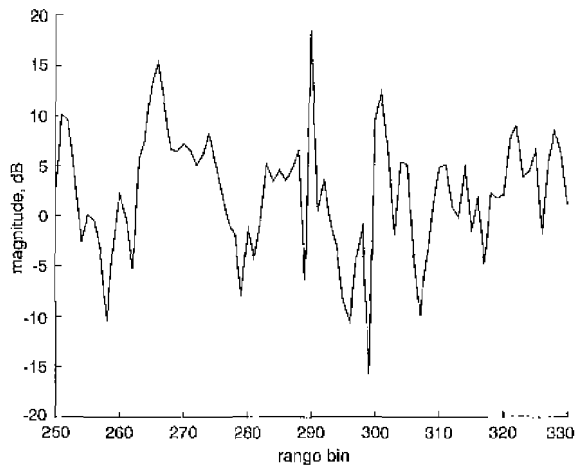

Fig. 10 *MSMI statistic against range using a Kaiser–Bessel window*

Table 2: Separation between statistic at target and the next highest statistic

Algorithm	Doppler	Improvement	Range	Improvement
JDL	3.13 dB	N/A	−8.73 dB	N/A
Modified JDL	8.39 dB	5.26 dB	2.49 dB	11.22 dB
JDL-windowed	8.80 dB	5.67 dB	3.13 dB	11.86 dB

4.2.2. Example 2. MTS tones: Flight 5 acquisition 152 includes clutter and tones from a moving target simulator (MTS) received at pre-selected Doppler frequencies. Five tones are received at approximately −800 Hz (0 dB), 600 Hz (−14 dB), −400 Hz (−20 dB), −200 Hz (−26 dB) and 0 Hz (−31 dB). The data in this acquisition are the returns from 128 pulses measured at 22 channels. Using the Global Position System (GPS) and inertial navigation unit data of the radar platform, the known location of the MTS source and the timing of the MTS pulse, it is possible to calculate the locations of the tones in range. The MTS generator is triggered by the transmit main beam and so the tones are in the transmit direction. For acquisition 152, the tones are located mainly in range bin 450 and about 6° degrees towards the nose. The pulse-repetition frequency for this flight was 1984 Hz, hence the

separation of 200 Hz corresponds to nearly 13 Doppler bins.

Using the acquisition with the MTS tones allows us to compare the performance of the JDL algorithm in the above scenarios on real data without any injected targets. The tones act as returns from moving targets. The presence of five MTS tones makes it difficult to define a single figure of merit to compare the different scenarios and so a visual inspection is used for comparison.

Fig. 11 plots the results of using a non-adaptive digital beamformer to locate the MTS tones in Doppler at the range bin and angle of the transmitter. The strongest tones at Doppler bins -52 and -39 are clearly visible over the clutter. The other 3 tones are visible but embedded in the surrounding clutter.

Fig. 12 plots the results of using the JDL algorithm without accounting for the non-orthogonality of the steering vectors. As can be seen, the five MTS tones are visible, with the strongest tone at bin -53 spread out over Doppler space. However, a few spurious tones are also seen. Fig. 13 plots the results of taking the non-orthogonality into account using eqn. 13. The five MTS tones all clearly stand out over the clutter and the spread of the strongest tone has been curtailed. The spurious tones are completely suppressed. Fig. 14 plots the case where the Kaiser–Bessel window is used to transform the time domain to the

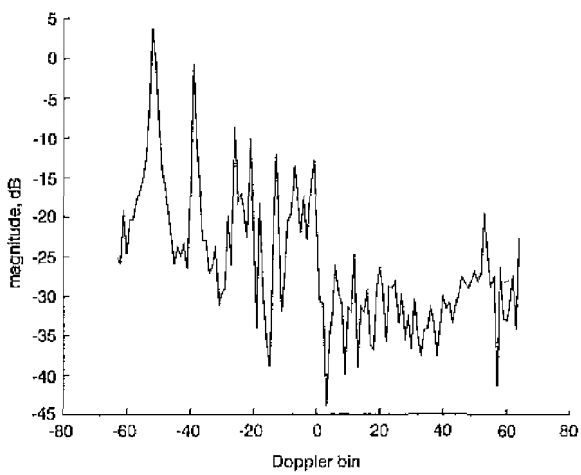

Fig. 11 *Location of the MTS tones using a non-adaptive beamformer*

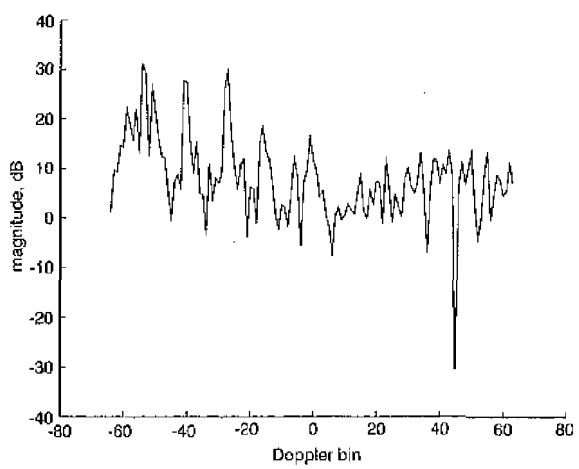

Fig. 12 *MTS tones ignoring non-orthogonality of steering vectors*

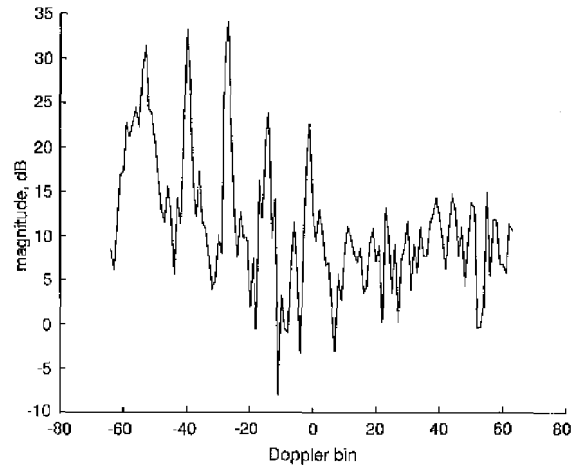

Fig. 13 *MTS tones accounting for non-orthogonality of steering vectors*

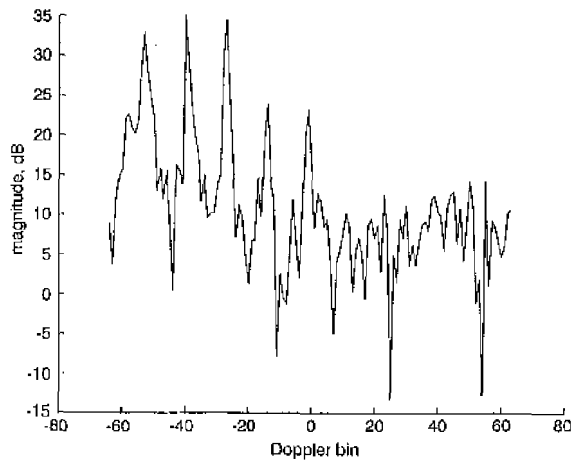

Fig. 14 *MTS tones using a Kaiser–Bessel window*

Doppler domain. Again, the five tones clearly stand out and the spread of the strongest tone is curtailed. This case shows some improvement over the case of Fig. 13.

5 Conclusions

The JDL processing algorithm, as originally developed by Wang and Cai [3], transforms space–time data to the angle–Doppler domain using a 2-D DFT. The DFT-based transformation restricts look angles and the spacing between the angle–Doppler bins in the transform domain. These restrictions are not explicitly stated in the original presentation. Furthermore, in practice, the spatial steering vector is affected by mutual coupling between the elements of the array. The DFT is not the appropriate transform from the space domain to the angle domain. In a practical case, spatial data must be transformed to the angle domain using an inner product with the corresponding measured steering vector. The spatial transformation is necessarily non-orthogonal, leading to spreading of target information in the angle domain.

This paper reformulates the JDL algorithm in terms of a general transformation matrix encompassing both the theoretical and practical scenarios. The formulation removes the restrictions placed on the original JDL algorithm.

Removing the restrictions on spacing between angle and Doppler bins significantly improves the performance of the JDL algorithm. Section 4.1 uses two examples to illustrate the improvement in the probability of detection for a given false-alarm rate. These examples use simulated data from an ideal array of point sensors. This allows for enough independent realisations for a reasonable Monte Carlo simulation. It must be emphasised that the choice of optimal spacing between angle and Doppler bins is yet an open research problem.

This paper also presents examples to illustrate the improvement in adaptive processing using measured data from the MCARM program. While earlier researchers have used measured steering vectors for the spatial transformation [5], the resulting spread in target information had been ignored. The formulation presented in this paper accounts for the spread, and yields significantly improved performance.

This paper also introduces, for the first time, a window in the transformation from the space–time domain to the angle–Doppler domain. In earlier publications on the JDL algorithm, the use of a window is explicitly discouraged because of the resulting spread in target information. However, since any target spread can be accounted for, it is possible to take advantage of the low transform sidelobes by using an appropriate window.

The key contribution of this new approach is the elimination of the two stipulations on the original JDL algorithm of [3] and the introduction of a matrix-based transformation to the angle–Doppler domain.

6 Acknowledgments

The authors would like to thank Dr. Yuhong Zhang of Stiefvater Consultants Inc., 10002 Hillside Terrace, Marcy, NY 13403, for providing us with the false-alarm rates for the chosen degrees of freedom, number of secondary data samples used, and thresholds in Section 4.

7 References

1 BRENNAN, L., and REED, I.: 'Theory of adaptive radar', *IEEE Trans. Aerosp. Electron. Syst.*, 1973, **AES-9**, pp. 237–252
2 HARRIS, F.: 'On the use of windows for harmonic analysis with the discrete Fourier Transform', *Proc. IEEE*, 1978, **66**, (1), pp. 51–83
3 JAFFER, A., BAKER, M., BALLANCE, W., and STAUB, J.: 'Adaptive space–time processing techniques for airborne radars'. Contract F30602-89-D-0028, Hughes Aircraft Company, Fullerton, CA 92634, July 1991
4 MELVIN, W.L., and HIMED, B.: 'Comparitive analysis of space–time adaptive algorithms with measured airborne data'. Proceedings of the 7th International Conference on *Signal processing applications and technology*, October 1996
5 REED, I.S., MALLETT, J., and BRENNAN, L.: 'Rapid convergence rate in adaptive arrays', *IEEE Trans. Aerosp. Electron. Syst.*, 1974, **AES-10**, (6), pp. 853–863
6 ROBEY, F.C., FUHRMANN, D.R., KELLY, E.J., and NITZBERG, R.: 'A CFAR adaptive matched filter detector', *IEEE Trans. Aerosp. Electron. Syst.*, 1992, **28**, pp. 208–216
7 SLOPER, D., FENNER, D., ARNTZ, J., and FOGLE, E.: 'Multi-channel airborne radar measurement (MCARM), MCARM flight test'. Contract F30602-92-C-0161, Westinghouse Electronic Systems, April 1996, Additional information available at http://sunrise.deepthought.rl.af.mil
8 WANG, H., and CAI, L.: 'On adaptive spatial-temporal processing for airborne surveillance radar systems', *IEEE Trans. Aerosp. Electron. Syst.*, 1994, **30**, pp. 660–699
9 WARD, J.: 'Space–time adaptive processing for airborne radar'. Tech. Rep. F19628-95-C-0002, MIT Lincoln Laboratory, December 1994